Robotica (2010) volume 28, pp. 719–735. © Cambridge University Press 2009
doi:10.1017/S0263574709990403

A methodology for static stiffness mapping in lower mobility parallel manipulators with decoupled motions

Charles Pinto*, Javier Corral, Oscar Altuzarra and Alfonso Hernández

Department of Mechanical Engineering, University of the Basque Country, 48013 Bilbao, Spain

(Received in Final Form: July 23, 2009. First published online: September 24, 2009)

SUMMARY

In this paper a general methodology for obtaining static stiffness maps in lower mobility parallel manipulators is proposed. The main objective is to define a set of guidelines, which allow the experimental work to be optimized and computational time to be reduced. First, a two-degree-of-freedom (DOF) mechanism will be used for methodology validation, since it is the stiffness of the basic kinematic chain of the manipulator that is to be analysed. Two mathematical models of this mechanism and an experimental prototype will be considered for the validation. After that, the methodology will be applied to a lower mobility (4-DOF) parallel manipulator. In this paper, the experimental prototype and its set-up is highly important because some particular features of the experimental analysis will be defined. This paper introduces a key experimental tool: the preload, which allows the clearances and possible assembling errors to be considered. The added value from the application of this procedure is the obtaining of graphs that describe, in an intuitive and useful way, the behaviour of the manipulator's stiffness inside its workspace as a function of the mobile platform position and orientation.

KEYWORDS: Parallel manipulator; Stiffness maps; Finite element method; Analytical model; Experimental set-up.

1. Introduction

Regarding the study of the static behaviour of robots in general, and parallel manipulators in particular, the stiffness characteristic is a critical issue and a very important factor in the performing of their applications. The main reason is that the specific tasks for which these manipulators are employed are related to activities requiring a high precision, like, for example, machining processes in which the surface finish is an important parameter; telescope positioning and orientation; microprecision tools in surgical applications and pick and place operations with high loads.

Parallel kinematics manipulators are usually mechanisms with a complex topology and configuration that make the definition of the static stiffness complicated and tedious. For this reason, throughout the work previously undertaken in this field, various methods have been used to define a mathematical model of equivalent stiffness that simplifies the definition of this property. Specifically, studies in this field have used several methods for the definition of stiffness models that are based on Jacobian matrix calculation, structural matrix analysis and the finite element method.

The definition of the stiffness model by means of the Jacobian matrix has evolved significantly from the first model,[1] in which stiffness maps were represented on the workspace of a Stewart platform considering the elasticity of the actuators and assuming rigid elements. And with this same approach, the values of stiffness based on the eigenvalues of the stiffness matrix (modulus of the stiffness) and the eigenvectors (corresponding stiffness directions) were proposed as an alternative stiffness evaluation.[2] In the subsequent papers,[3–7] deformation in the legs affecting the positioning of the manipulator is also considered. To achieve this, the static behaviour of each leg is analysed and, later, coupling these effects with the aid of the Jacobian matrix, the whole model of the manipulator is studied. In this way, several lumped models are defined in which elastic elements are converted into rigid elements with an equivalent stiffness in the active joints. The main limitation of this approach is that the applicability of the method is only valid in those cases in which the manipulator has no redundant constraints.[7] In addition, given the differential nature of the Jacobian matrix, the movements induced by the deformations must be in the rank of small displacements since they have to be compatible with the kinematic restrictions inherent to the use of the Jacobian. This approach has been widely used to evaluate the stiffness behaviour in redundantly actuated parallel manipulators.[8] The improvement of the stiffness with an extra leg is stated by a comparison of the moving platform deflections between two examples with and without actuation redundancy. In order to evaluate the weak points of its design, also by means of the overall Jacobian matrix, the stiffness for the Tricept robot is analysed.[9] In this paper, the use of two global indices from the singular value decomposition of the stiffness matrix is proposed.

On the one hand, when models based on the structural matrix analysis are used, the technique consists in the definition of the stiffness matrix for each element in local coordinates based on the efforts supported by each leg. Then, by means of the transformation matrix between reference systems, the matrix of the element in global coordinates is defined and finally, through the nodes connectivity, the full set is assembled. In types of manipulators composed of several identical legs the work can be simplified remarkably, since once one leg is solved, the others can be defined in an analogous way and only the assembly stage, by which the stiffness matrix of the set is defined, remains

* Corresponding author. E-mail: charles.pinto@ehu.es

https://doi.org/10.1017/S0263574709990403 Published online by Cambridge University Press

to be completed. Under this approach, a model[10] of the Gough–Stewart platform with the deformation of the set associated to the arms has been defined; in this approach, a mobile platform with a comparatively greater stiffness than the rest of elements is presented and, finally, with the aid of Gaussian elimination the model is solved. Along the same lines, another model is developed[11] in which, after obtaining the stiffness matrix, a function of potential energy is defined and its minimum solved subject to kinematic restrictions imposed by means of Lagrange's multipliers. In this same paper, but in a second version of the model, some of the kinematic restrictions are replaced by stiffness matrices, with elements of an empirical origin, that allow the stiffness in the joints to be considered. As some models cannot distinguish between the situations in which the manipulator has a very low stiffness along certain directions, a Jacobian-based analysis considering the minimum and maximum stiffness and its variance as reasonable indices for stiffness evaluation was proposed.[12] This paper provides a helpful methodology for the design stages of the manipulator. The main contribution is the stiffness model in relation to which the centre of stiffness and the compliant axis are defined. Even frame deformations can be considered,[13] where, under linear superposition principle assumptions, not only the manipulator stiffness but also the machine frame compliance is analyed. Other approaches[14,15] present models based on structural analysis to provide an easy and systematic method to calculate the analytical stiffness matrix of parallel manipulators whose structures are made with slender links. These models are built with beam elements; the results are presented along the three Cartesian directions where joint stiffness can also be considered. The originality of the method lies in well-suited models that allow joint stiffness and the manipulator's own weight to be considered. Then a finite model is introduced to verify the results obtained through the derived model.

On the other hand, there are models developed by means of the finite element method (FEM). This kind of model adequately describes the real behaviour and if the computer aided design (CAD) geometry is available from the design stage the process of building such a model is fairly straightforward. Nevertheless, the weak point of these models is their necessity to be meshed in each one of the postures analysed, becoming thus, a tedious and computationally expensive task. Some authors use these models to correlate with other proposed approaches and to validate their method. For a Gough–Stewart platform with flexible legs and rigid platform[2] a study was carried out by means of different Young's moduli. In another approach to stiffness analysis[7] implemented for the Orthoglide parallel manipulator, the authors define a finite element-based model for only one correlation position. The validation stage introduces the FEM to verify the results obtained through the structural analysis[11] and also a finite element model[16] is utilized for the correlation with the experimental results, in which authors evaluate the stiffness at a single point of the workspace. The model is built with beam elements and the results are presented for the three Cartesian directions of application of the force. Likewise, a finite element-based model of the manipulator can be applied for the validation of a mathematical model.[17]

These modelling methods need a practical validation that it is made by means of experimental testing on a prototype. In another study,[18] the static behaviour evaluation of a robot is analysed by means of norms ANSI/RIA R15.05-1-1990[19] and ISO 9283:1998[20] which are established for serial manipulators. There are also cases[8] where the experimental tests are made on the basis of an american society of mechanical engineers (ASME) norm[21] for computer numerical control (CNC) machining. The stiffness of the manipulator is analysed by means of force gauges, which measured deformations are caused by imposing displacements in the mobile platform. The distribution of the measurement points is found along two measurement planes, based on the symmetry of the workspace. In this work, the standard deviation of the repeatability for three measurements made at a point is reported. For other experimental tests,[14] the applied load is 200 N in the vertical direction and downwards. Measurements are made in two different planes of the workspace and the induced deformations are also obtained, by means of dial indicators with a resolution of 1 μm. Some experimental measurements[16] reveal the stiffness results for a single point corresponding to the application of a load along the three Cartesian directions, with values of the load between 10 and 50 N. Finally, a model of specific stiffness has been developed for a high speed machining machine[22] based on the technique of experimental design of experiments (DOE),[23] obtaining stiffness maps for some planes in which the variation of the stiffness is presented along Cartesian directions.

In the following sections, a stiffness mapping methodology is set out and its validation on a 2-DOF representative mechanism is demonstrated. After this validation, a 4-DOF spatial parallel manipulator case is derived and finally, based on the results obtained, the most important conclusions are presented.

2. Stiffness Analysis Methodology

In this section, a procedure for the definition of a systematic stiffness obtaining procedure within the workspace of a manipulator is established. To achieve this, a cycle of work defined by the flowchart of Fig. 1 is carried out. The procedure established by this chart is the following:

1. Mobility analysis and DOF nature: at this point, the kinematics of the manipulator is analysed. One of the basic characteristics is the number and nature (translational or rotational) of the DOF of the mobile platform, necessary to obtain the dimension of the workspace in which it operates.
2. Solution of the position problem: from the closed loop equations of the mechanism, the inverse kinematic problem (IKP) as well as the direct kinematic problem (DKP) are solved. This task is essential for obtaining the manipulator's workspace. The real workspace is the one associated with the selected working mode[24] that remains invariable for all the poses.
3. Model development: there are two possible approaches, the mathematical and the experimental one. If an experimental prototype is available, its results are taken

https://doi.org/10.1017/S0263574709990403 Published online by Cambridge University Press

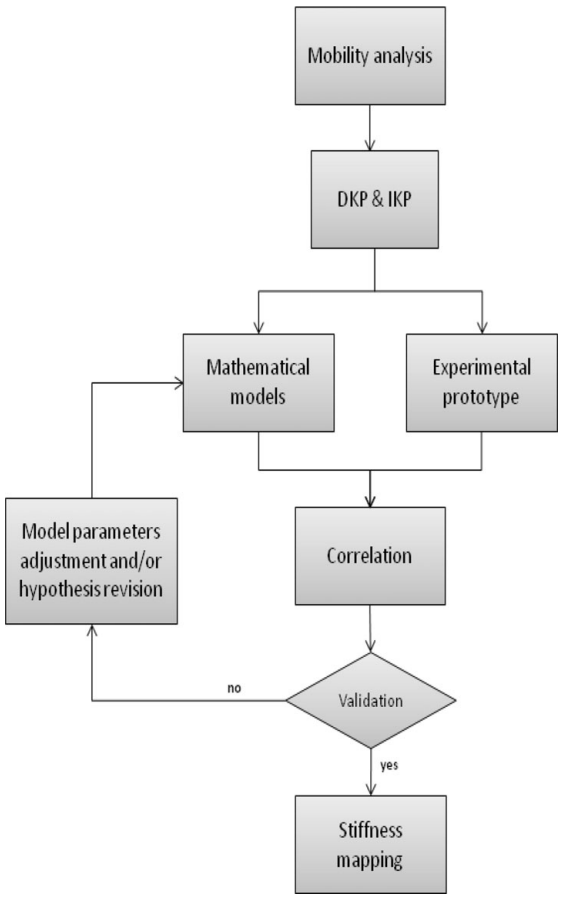


Fig. 1. Methodology diagram.

as a reference for the refinement and validation of the mathematical models.

4. Correlation and validation: from the results obtained in these models and prototype a correlation between them is made to ascertain whether the models are correct or, on the contrary, it is necessary to refine them from the point of view of the working modes of the links or the compliant elements considered (links, joints, etc.).
5. Stiffness maps: consisting in three-dimensional figures in which the variation of the static stiffness is depicted for the whole workspace. In these maps it is possible to visualize the engineering stiffness as a function of the mobile platform DOF through the workspace, resulting in practical information for the end user or in the design stages of the manipulator.

3. Methodology Validation

In the following section, the methodology described above will be applied to a planar mechanism following the procedure reflected in the flowchart in Fig. 1. The kinematic chain proposed for the methodology validation has been specifically selected because it is the basic chain of each leg forming the complete three translations and one rotation (3T1R) manipulator of Section 4. The global stiffness will be determined by the assembly of these leg substructures as the sum of the legs' stiffness and the mobile platform compliance. Within this work, linear behaviour of the material is assumed.

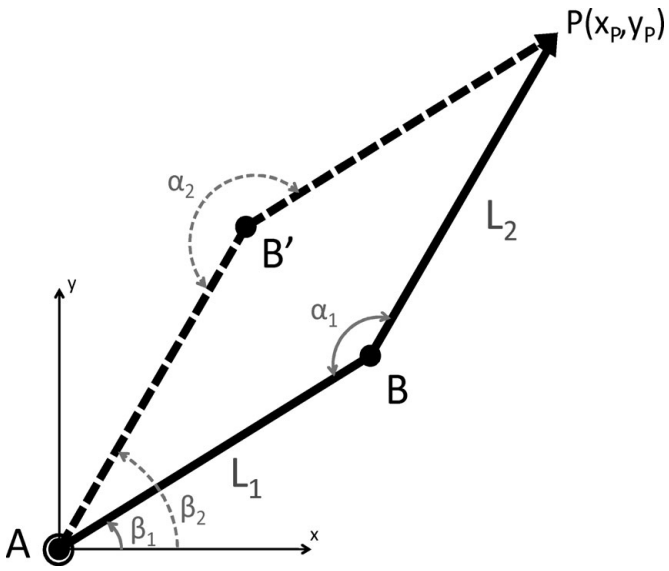


Fig. 2. Mechanism configurations.

3.1. Two rotation manipulator

The 2R manipulator consists of two elements connected by means of a revolute joint. One of them is also connected to the fixed element by means of another revolute joint as shown in Fig. 2.

The two DOFs are: a rotation defined by the parameter β in its connection to the fixed element and the rotational joint between both mobile elements defined by the angle α.

The element connected to the fixed element, made of aluminium (see Table I for details), is 0.624 m long and weighs 0.996 kg. The second one is made of the same material, also 0.624 m long and it weighs 1.069 kg.

3.2. Direct kinematic problem and inverse kinematic problem

For the resolution of the position problem the closed loop equations are

$$\overrightarrow{AP} = \overrightarrow{AB} + \overrightarrow{BP}. \tag{1}$$

By decomposition of the vector into its components yields

$$x_p = L_1 \cdot \cos\beta + L_2 \cdot \cos(\beta + \pi - \alpha), \tag{2}$$

$$x_p = L_1 \cdot \sin\beta + L_2 \cdot \sin(\beta + \pi - \alpha), \tag{3}$$

where L_1 and L_2 are the lengths of the two bars, $\overline{AB}$ and $\overline{BP}$ respectively.

Table I. Links material properties.

Material	Aluminum
Young modulus (E_{Al})	68.9 GPa
Shear modulus (G_{Al})	25.8 GPa
Density	2,710 kg/m^3

https://doi.org/10.1017/S0263574709990403 Published online by Cambridge University Press

Equations (2) and (3) define the DKP. Once α and β parameters are known, the position of the mobile platform $(x_P; y_P)$ can be obtained.

For the IKP, a transformation between Eqs. (2) and (3) is necessary. Summing their squares, angle α is obtained:

$$\alpha = arc\cos\left(\frac{L_1^2 + L_2^2 + x_p^2 - y_p^2}{2 \cdot L_1 \cdot L_2}\right). \tag{4}$$

If two different roots are obtained from Eq. (4), α_1 and α_2 represent the two possible configurations of the mechanism shown in Fig. 2. In the case of one double root the mechanism is in a fully stretched or folded configuration corresponding to a singular position.

Coordinates of point B point are obtained as the intersection of two circumferences of known radii (L_1 and L_2) and centre points (A and P respectively) leading to the two possible solutions for angle β:

$$\beta = arc\tan\left(\frac{y_B}{x_B}\right). \tag{5}$$

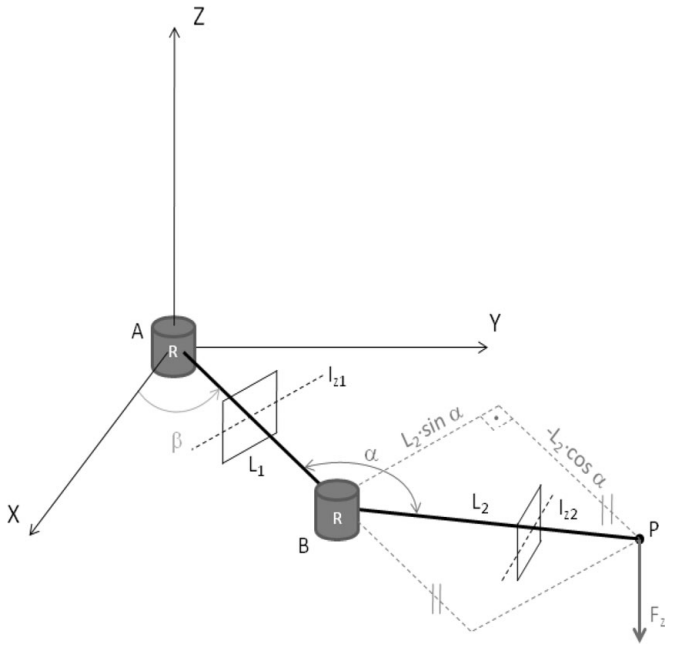


Fig. 3. R-dyad model parameters.

3.3. Stiffness analysis

Following paragraphs present two mathematical models, the first one analytical and the second numerical. In this case, an experimental prototype is also available to analyse the stiffness behaviour of the leg. This study is limited to the analysis of the static stiffness when the applied force has a single component along the z direction (perpendicular to the plane containing the 2R mechanism), therefore, only the elements of the **K** stiffness matrix related to a vertical application of the load, that is to say, k_{zx}, k_{zy}, k_{zz} and the symmetrical k_{xz} and k_{yz}, are considered.

3.3.1. Elastic model. The following model is based on the behaviour of prismatic elements that is described within the theory of elasticity.[25] Element $\overline{AB}$ is defined by its length L_1 and section A_1, the Young's modulus E_{Al}, the shear modulus G_{AL} and the second order inertia moments of the section I_{z1} and I_p. Similarly, element $\overline{BP}$ is defined by its properties: L_2, A_2, and E_{Al} plus only the second-order moment of inertia of the section I_{z2} since its working mode is exclusively bending.

Figure 3 illustrates the geometric dimensions required for the calculation of deformation obtained at point P. The connection of $\overline{AB}$ to the fixed element (joint A) is a revolute joint located at the origin of the reference system with its axis in a vertical direction. Next, this first mobile element of the R-dyad is additionally connected to the second element of the mechanism ($\overline{BP}$) by means of another vertically oriented revolute joint (B). The position variation of the P point is the effect of the z direction applied unit force. Since they will help to simplify the calculation of the displacements in the following stages, the geometrical projections of the second element along the direction of the first one appear in Fig. 3.

From these initial considerations the proposed model is analysed. The connection with the fixed element is modelled by a clamping boundary condition and rotation in the revolute joint in B is also blocked. In order to evaluate the static behaviour, the components of the displacement of P according to the different working modes are obtained and, later, by means of the superposition principle the total displacement is calculated. The direction of application of the force is parallel to the axes of the revolute joints (z direction) and downwards, and the application point is P. Under these load conditions, element $\overline{AB}$ works under bending and torsion, whereas $\overline{BP}$ element works under only bending. On the other hand, the compliance of the joint axis is also considered to improve the accuracy of the model.

The first compliant element is the axis of the joint connecting the R-dyad to the frame. This axis is made of steel (see properties in Table II).

The load applied at point P makes this axis behave like a simply supported beam under a bending moment applied at its middle point. In Fig. 4, the shape of the joint axis in its non-deformed position is presented. Classical formulation of this problem[25] allows λ_0 deflection angle to be obtained which causes a displacement δ_0 of point P given by

$$\delta_0 = \frac{M_0 \cdot L_a}{24 \cdot E_{st} \cdot I_a} \cdot (L_1 - L_2 \cdot \cos\alpha), \tag{6}$$

where M_0 is the equivalent bending moment, and in this case

$$M_0 = L_1 - L_2 \cdot \cos\alpha. \tag{7}$$

Note that for this axis only the plane containing the link L_1 bending has been considered. The axis working mode

Table II. Axis material properties.

Material	Steel
Length (L_a)	0.1 m
Diameter	$8{\cdot}10^{-3}$ m
Young modulus (E_{st})	210 GPa

https://doi.org/10.1017/S0263574709990403 Published online by Cambridge University Press

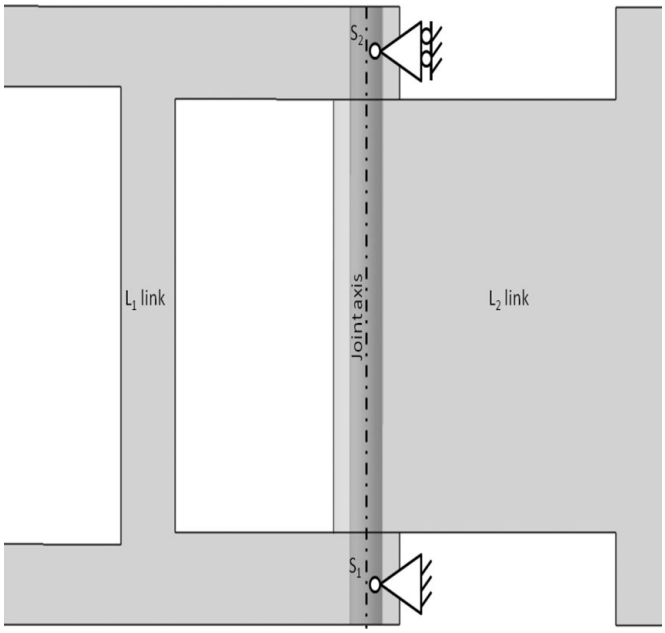


Fig. 4. Fixed frame connection axis.

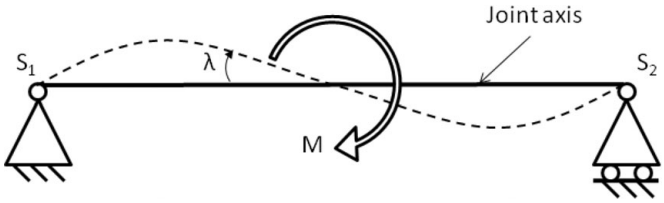


Fig. 5. Simply supported beam. Joint deformation.

is given by the simply supported beam model presented in Fig. 5.

Due to the $\overline{AB}$ bending, there is a first component δ_1 of the total displacement. Considering a unitary load, the displacement δ_1 is determined by

$$\delta_1 = \frac{L_1^3}{3 \cdot E_{Al} \cdot I_{z_1}} - \frac{L_1^2 \cdot L_2 \cdot \cos\alpha}{2 \cdot E_{Al} \cdot I_{z_1}}. \tag{8}$$

Moreover, as a consequence of this bending effect there is a reorientation θ_B of the section in B that results in a rigid solid movement in $\overline{BP}$ and it gives rise to an additional downwards displacement the value of which is $\delta_2 = \theta_B \cdot \overline{BP}$, where

$$\delta_2 = \frac{L_1 \cdot L_2^2 \cdot \cos^2\alpha}{E_{Al} \cdot I_{z_1}} - \frac{L_1^2 \cdot L_2 \cdot \cos\alpha}{2 \cdot E_{Al} \cdot I_{z_1}}. \tag{9}$$

As stated for the previous joint, the axis of the rotational joint behaves like a simply supported beam under the action of a bending moment at its middle point (see Fig. 5). This axis bending results in an additional displacement of the P point, the value of which is the angle λ of the deformed shape of the axis times the projected length of the second link. The main geometrical characteristics of the axis are presented in Table II. In this case, the length of the link is L_2 projected onto the two possible planes of the joint axis bending.

Given the resulting deformed shape of the axis, the angle λ is obtained as in the previous case. The angles in the two directions of bending are

$$\lambda_{22} = \frac{M_{22} \cdot L_a}{24 \cdot E_{st} \cdot I_a}, \tag{10}$$

$$\lambda_{32} = \frac{M_{32} \cdot L_a}{24 \cdot E_{st} \cdot I_a}, \tag{11}$$

where M_{22} and M_{32} stand for the corresponding bending moments in each plane and have the following values:

$$M_{22} = -L_2 \cdot \cos\alpha, \tag{12}$$

$$M_{32} = L_2 \cdot \sin\alpha. \tag{13}$$

The resulting displacement addends are

$$\delta_{22} = \lambda_{22} \cdot L_2 \cdot (-\cos\alpha), \tag{14}$$

$$\delta_{32} = \lambda_{32} \cdot L_2 \cdot \sin\alpha. \tag{15}$$

The torsion effect in element $\overline{AB}$ gives a third displacement δ_3 of point P:

$$\delta_3 = \frac{L_1 \cdot L_2^2 \cdot \sin^2\alpha}{G_{Al} \cdot I_p}. \tag{16}$$

Finally, δ_4, the displacement from the element $\overline{BP}$ bending effect and the modulus, is given by Eq. (17):

$$\delta_4 = \frac{L_2^3}{3 \cdot E_{Al} \cdot I_{z_2}}. \tag{17}$$

Applying the superposition principle, the total deformation expression is obtained:

$$\delta_{\text{Tot}} = \delta_0 + \delta_1 + \delta_2 + \delta_{22} + \delta_3 + \delta_{32} + \delta_4. \tag{18}$$

The value of the k_{zz} component for the analytical model is

$$k_{zz} = \frac{1}{\delta_{\text{Tot}}}. \tag{19}$$

3.3.2. Finite element-based model. The finite element-based model has been obtained from the original geometrical set. The material is aluminium Al 1100-H14 and the model has approximately 27,700 second-order tetrahedral elements. The restrictions prevent both possible rotations in the R-dyad and with respect to the fixed element a clamping boundary condition is used. The load is a 20 N downwards vertical force. In Fig. 6, CAD model of the R-dyad in a particular position of the parameter ($\alpha = 140^\circ$) appears with the constraints and the fixed boundary condition at the right end.

Figure 7 shows the deformed shape of the set with the distribution of the displacements throughout the mechanism. It can be observed that the greatest displacements are on the left side (load application point).

From this deformations analysis, the response of the numerical model for the following positions of the set based on α has been obtained, and the result is shown later in the corresponding validation section.

https://doi.org/10.1017/S0263574709990403 Published online by Cambridge University Press

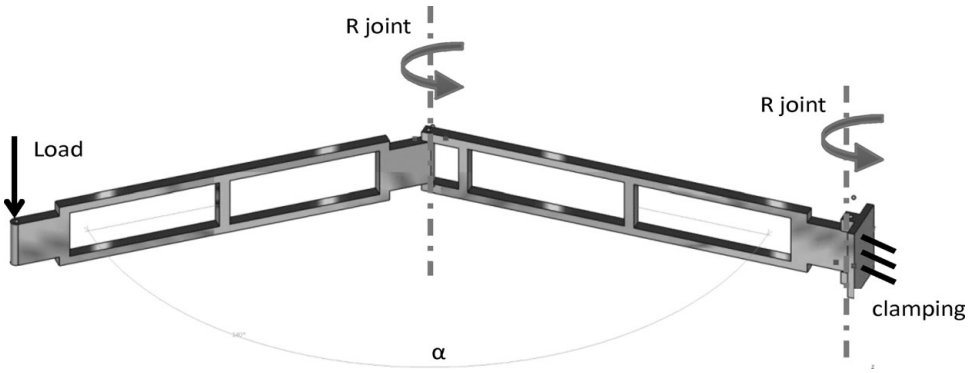


Fig. 6. *R*-dyad CAD model with constraints.

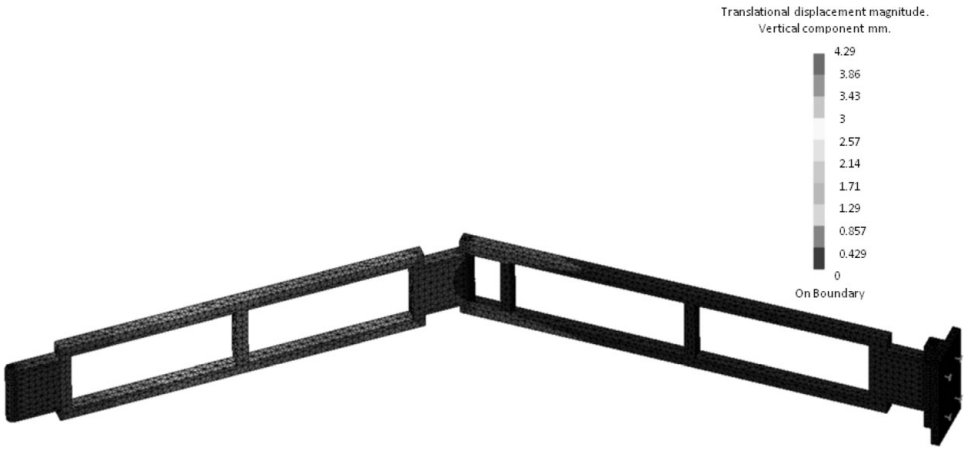


Fig. 7. FEM model deformed shape.

3.3.3. Experimental prototype. Once the mathematical models have been presented, the following step is to analyse the static behaviour in the vertical direction of the experimental prototype. Figure 8 depicts the experimental prototype, the equipment used in the experimental measurements and masses for application of the loads.

The procedure for carrying out the experimental stiffness analysis consists of the elemental steps shown in the flowchart presented in Fig. 9. Each level of the block diagram gives details for a correct and accurate measurement process related to the *R*-dyad experimental testing.

Step 1. Experimental measurement definition: once the workspace of the manipulator is known, a representative number of measurements, their spatial distribution and the measurement order are defined. As the connection is by means of a revolute joint, the measurements are placed every 10° along a semi-circumference. Theoretically, there should be a total of 18 measurements, but it is possible that some physical limitation such as interferences or contacts may vary this number.

Step 2. Manipulator localization: by means of the control system or by manual placement, the current position to be measured is fixed.

Step 3. The preload: in the manufacturing process and later assembly of the prototype certain errors are introduced as a consequence of the tolerances and the adjustments that give rise to gaps between the elements of the prototype. For this reason, nonlinearities can be produced in the realization of the experimental test. In order to avoid these undesirable displacements, a preload is applied in the system so that measurements represent the resistant behaviour of the system in a realistic way. The purpose of this preload is to eliminate

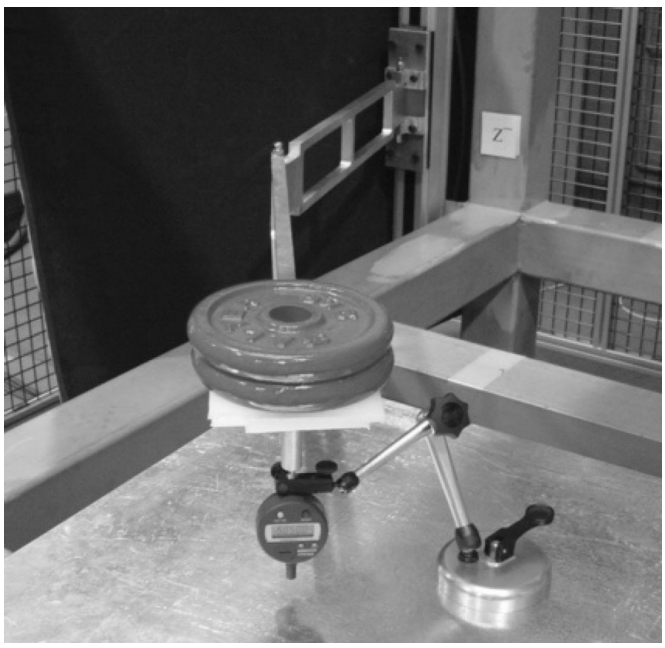


Fig. 8. Experimental measurements set-up.

https://doi.org/10.1017/S0263574709990403 Published online by Cambridge University Press

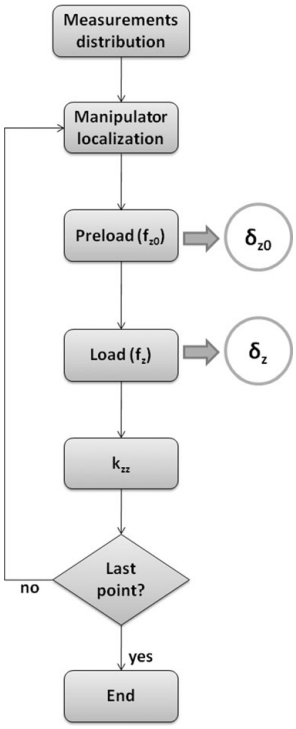


Fig. 9. Measurements cycle.

the gaps and to consider the aforementioned errors measuring the total displacement from a reference displacement (δ_{z_0}) induced by such a preload.

The preload required has to be ascertained experimentally and is the smallest value that makes the f_{z_0}/δ_{z_0} ratio constant. The stiffness is not a constant value for the lowest values of the preload due to the small rigid solid movements caused by gaps and friction due to assembling and manufacturing errors. For a given position of the prototype successive experimental tests to determine the optimal value of the preload have been made. Each test has consisted in loading the model with lumped values of the load from 10 to 90 N and measuring the resulting displacements in each fixed position. The result of this initial experimental test appears in the Fig. 10.

Considering the trend of this curve, the value of the preload is fixed at 30 N, which makes the stiffness effectively constant. Once the preload has been defined, the measurements are carried out according to Step 4. For this test a total load of 50 N has been selected: 30 N for the preload and 20 N more for the full load.

The magnitude $k_{zz}(\alpha)$ for the *R*-dyad is determined from expression (20) in the linear range,

$$k_{zz} = \frac{f_z - f_{z_0}}{\delta_z - \delta_{z_0}} = \frac{\Delta f_z}{\Delta \delta_z}, \tag{20}$$

where f_{z_0} and δ_{z_0} are the value of the preload and the resulting displacement, and f_z and δ_z are the total force applied and the absolute displacement respectively.

Once the measurement position is defined, the application of the preload and measurement of the initial displacement are carried out. The initial position of measurement is reached, that is to say, the one that is obtained as a result of the adjustment for the gaps and/or possible assembling errors. The displacement caused by the preload is measured and recorded for later use.

Step 4. Full load: in this step, the value of the total displacement (δ_z) is obtained for the whole load.

Step 5. Obtaining the element k_{zz} : by means of the following procedure, the engineering stiffness (when the load and the displacement are in the same direction) of the experimental prototype for different values of α is obtained. The application of the load in the z direction can produce moments and these give rise to deformations in the cross-sectional plane to the direction of the load. In Fig. 11, the displacements caused by the vertical load in the three directions as well as their averages are shown, for a sample of twenty measurements. From the data shown in Fig. 11, it is possible to deduce that the average displacements in the directions transverse to the direction of the load are an order of magnitude smaller than that aligned with the load and, consequently, they are not considered further in this work.

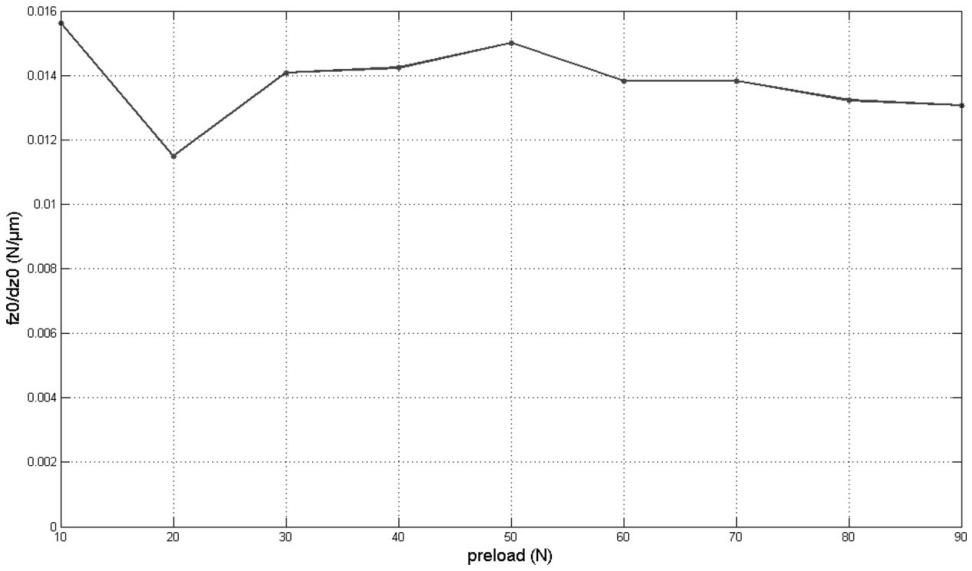


Fig. 10. Preload selection graph.

https://doi.org/10.1017/S0263574709990403 Published online by Cambridge University Press

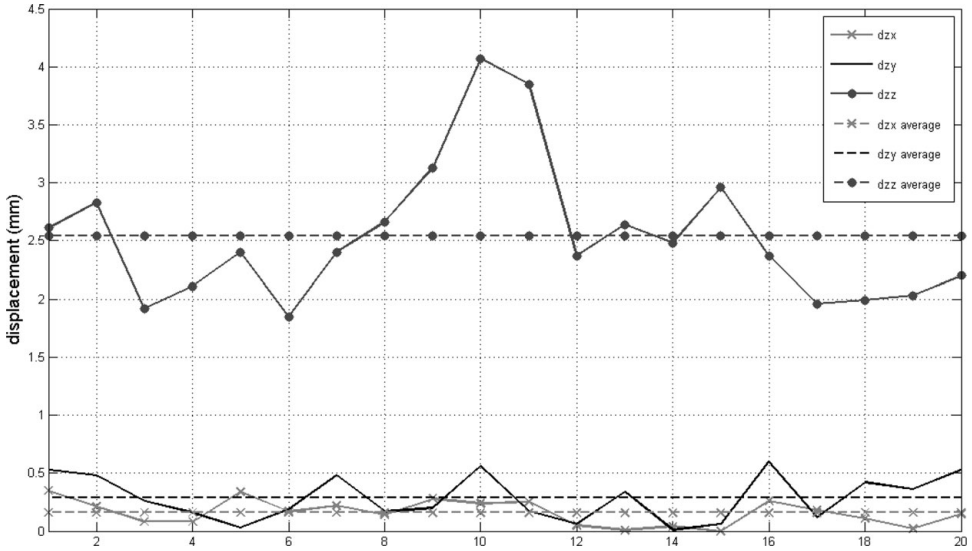


Fig. 11. Displacements components comparison.

In order to obtain the behaviour of the experimental prototype of the *R*-dyad, the previously presented procedure is repeated in whole the workspace and, from these values, the k_{zz} stiffness component is obtained.

3.4. Correlation and validation

From the various addends that compose the total displacement (δ_{Tot}), a graph of stiffness as a function of the parameter α can be plotted. Figure 12 shows that the interval of variation of the parameter has been limited to the range [23°, 160°]. The lower limit is imposed by the geometry of the physical model. For angles smaller than 23° there is interference between the elements of the prototype. The upper limit has been fixed as a representative value within the border of the workspace, avoiding the condition of alignment of the bars. The analytical model as set out in Eq. (19) is represented by a dashed line.

To validate the methodology, Fig. 12 presents the stiffness values of the proposed models versus those of the experimental prototype (continuous line). In the range of variation of the parameter α, the models have a trend of variation analogous to that of the prototype. Indeed between the curve of the analytical model and the one of the prototype there is an almost constant offset; the analytical model predicting a less rigid behaviour than the real one.

In contrast, the curve of the FEM model is practically superposed on the one of the real prototype; therefore, this is a model that faithfully predicts the behaviour of the prototype. However, with both models and the prototype it is possible to observe that the variation trend is analogous, all presenting a

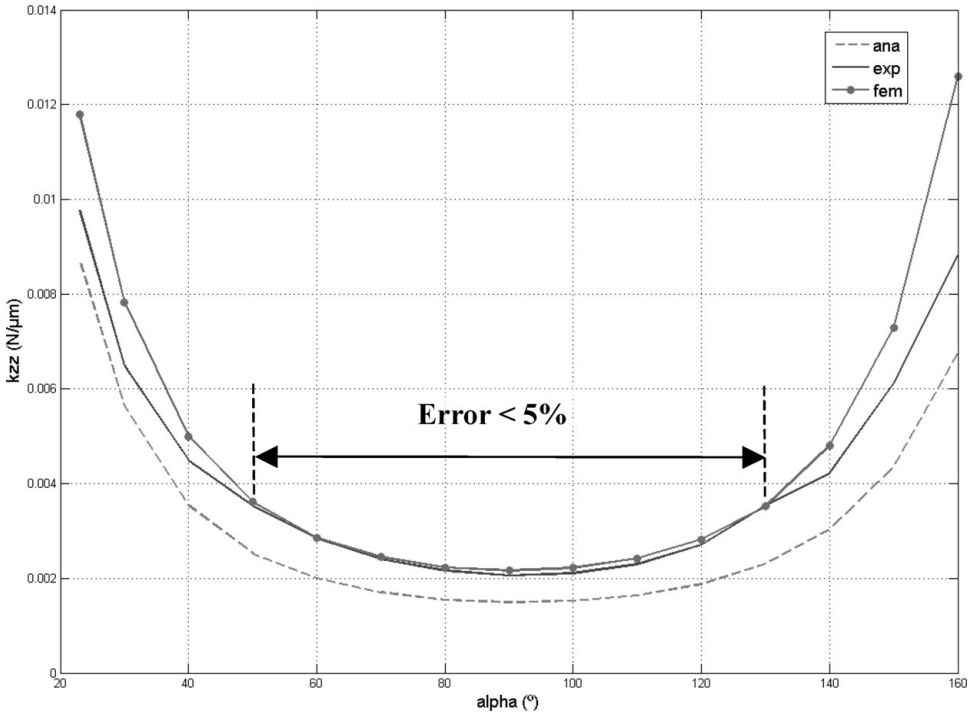


Fig. 12. *R*-dyad stiffness models correlation: $k_{zz}(\alpha)$.

https://doi.org/10.1017/S0263574709990403 Published online by Cambridge University Press

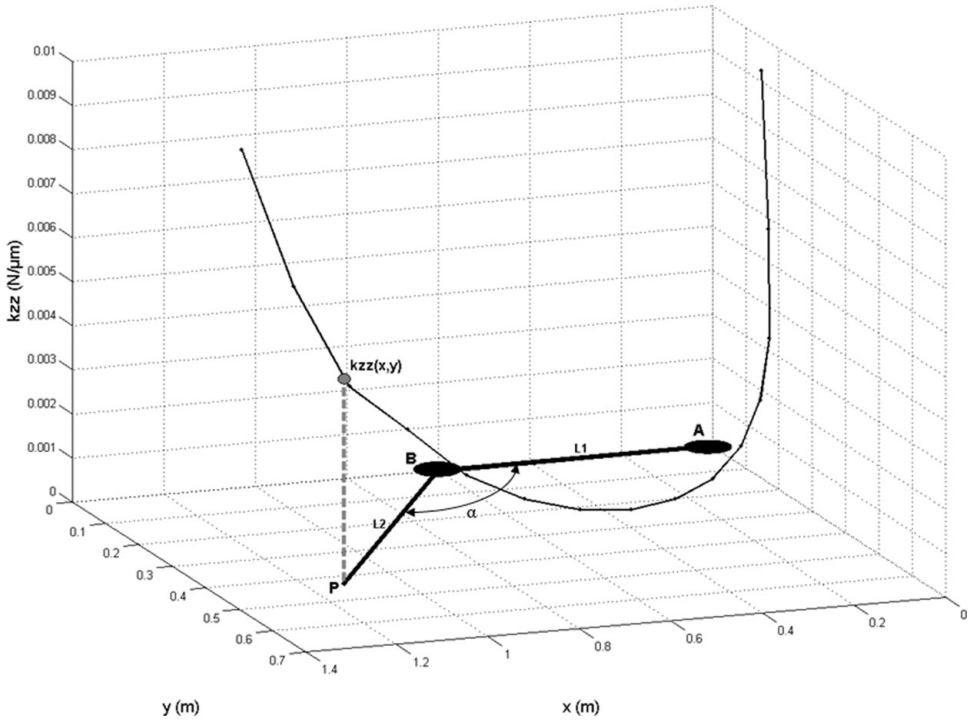


Fig. 13. Three-dimensional experimental stiffness map for R-dyad mechanism: $k_{zz}(x,\ y)$.

stiffness minimum at a value of $\alpha = 90^{\circ}$. This is mainly due to the influence of the torsion component of the displacement. When the bars are perpendicular the torsion moment arm is at a maximum and consequently the deformation is greater. On the contrary, when the bars are aligned (extended or folded) the effect of the torsion is smaller and consequently the stiffness is greater.

Both models give responses with a trend very close to that resulting from the experimental testing. An analysis of the average and relative error variation between the models and the prototype has been carried out. In the case of the FEM model, for the majority of the range [50°, 130°] the error does not exceed 5%. In this model, it has been assumed that the kinematic joints are ideal and the influence of this in the cases in which the bars are nearly aligned seems to be greater, given that it is in the limits of the range that the difference between the FEM model and prototype is the greatest. This influence is most noticeable in these cases because the working mode is bending and the arms work better in this mode. For the analytical model something similar occurs. However, although the error with respect to the prototype is greater (26%), the variation trend is more accurate than in the former model. In this case, the analytical response represents the stiffness trend almost exactly but scaled by a factor that leads to a constant offset between both responses across the range. To sum up, the R-dyad 3D stiffness map in its workspace is presented in Fig. 13. This provides the user with a more realistic view of the stiffness, since it is plotted within the workspace, i.e. $k_{zz}(x,\ y)$.

As can be deduced from the results presented in this section, with the experimental results taken as a reference, the FEM model obtains very accurate results across a large part of the variation range, whereas the analytical model predicts the trend correctly with a constant offset along the entire range. Both mathematical models have reasonable results so it can be stated that the methodology for the obtaining stiffness maps has been validated.

4. Case Study

In the following paragraphs, the study of a 3T1R 4-DOF parallel manipulator prototype is presented. The main application of the so-called DAEDALUS I manipulator consists in pick & place operations where the principal external loads are in a vertical z direction. This fact justifies the detailed study of k_{zz} on this manipulator.

4.1. 3T1R manipulator

DAEDALUS I robot (Figs. 14 and 15) is a lower mobility parallel kinematics manipulator.[26] The inputs are the prismatic joints and the motion pattern of the mobile platform is defined by 3T1R around a fixed direction. It comprises a fixed frame, a mobile platform and four identical legs connecting them. Each leg consists of the 2R kinematic chain previously analysed, connected to the mobile platform by means of another revolute joint. In addition, all the revolute axes of each leg are parallel.

4.2. Direct and inverse kinematic problem

The equations for the solution of the direct kinematic position problem are detailed in previous papers.[26] For the sake of convenience, the summarized results are presented here:

$$\begin{aligned} X_p &= X, \\ Y_p &= Y, \\ Z_p &= \frac{Z+U}{2}, \\ \theta &= \arcsin\left(\frac{Z-U}{d}\right), \end{aligned} \tag{21}$$

https://doi.org/10.1017/S0263574709990403 Published online by Cambridge University Press

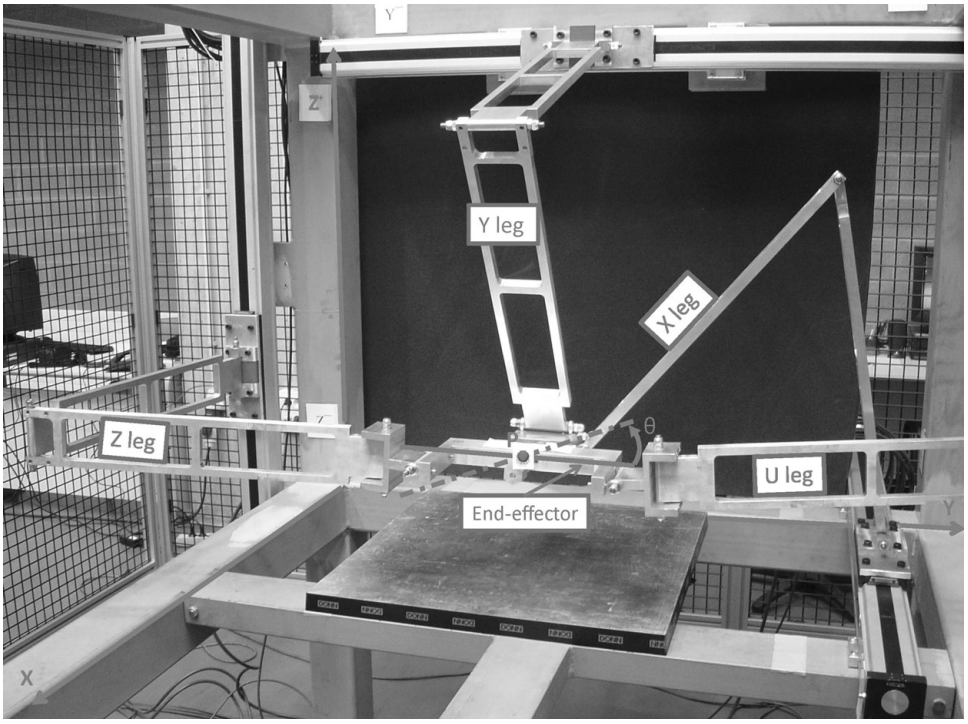


Fig. 14. DAEDALUS I prototype – 4-DOF parallel manipulator.

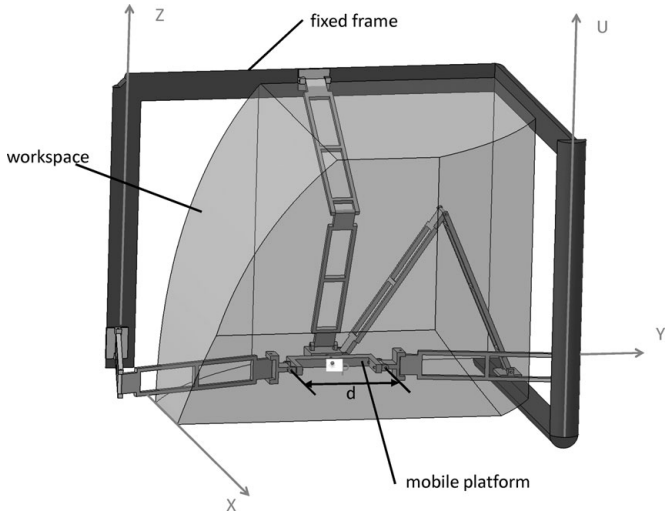


Fig. 15. DAEDALUS I manipulator workspace.

where (X, Y, Z, U) are the inputs, (X_p, Y_p, Z_p, θ) are the coordinates which define the position and the orientation of the mobile platform and d is the length of the mobile platform, as shown in Fig. 15.

The inverse kinematic problem equations are

$$\begin{aligned} X &= X_p, \\ Y &= Y_p, \\ Z &= Z_p + \frac{d}{2} \cdot \sin\theta, \\ U &= Z_p - \frac{d}{2} \cdot \sin\theta. \end{aligned} \tag{22}$$

From these equations and the length of the links, the workspace of the manipulator presented in Fig. 15 is obtained. The definition of the workspace is fundamental to decide the distribution of the experimental measurements as well as the order in which they are to be made. In Fig. 18, a top view of the workspace is also presented.

4.3. *Stiffness analysis*

The global stiffness of the complete manipulator is obtained as a result of the legs mounted in parallel plus the compliance of the mobile platform.

4.3.1. Experimental prototype. In this section, an experimental procedure for obtaining the manipulator stiffness within its workspace is presented. First, a methodology for measurements based on the characteristics of the manipulator is analysed. With the measurement devices in this experimental method, the k_{zz} element of the **K** stiffness matrix is obtained. This element provides information on the stiffness of the manipulator when the load is applied in the vertical direction (f_z). As presented in Fig. 16, the instrumentation for the experimental measurements comprises a 0.1 degree resolution inclinometer and a 0.01 mm resolution dial indicator. Both of them calibrated and specified according to standards.[27] Their working temperature range is $[-10^{\circ}\text{C}, +60^{\circ}\text{C}]$. Test laboratory conditions were approximately 1 atm and 20°C.

The cycle of the measurements is the same as explained in Section 3.3.3, and the preload in this case is 40 N (see Fig. 17).

Once the measurement position of the prototype is established by means of the control system, the installation of the measuring devices is set and each one of the experimental tests is carried out following the steps established in the Section 3.3.3. The experimental measurements have been

https://doi.org/10.1017/S0263574709990403 Published online by Cambridge University Press

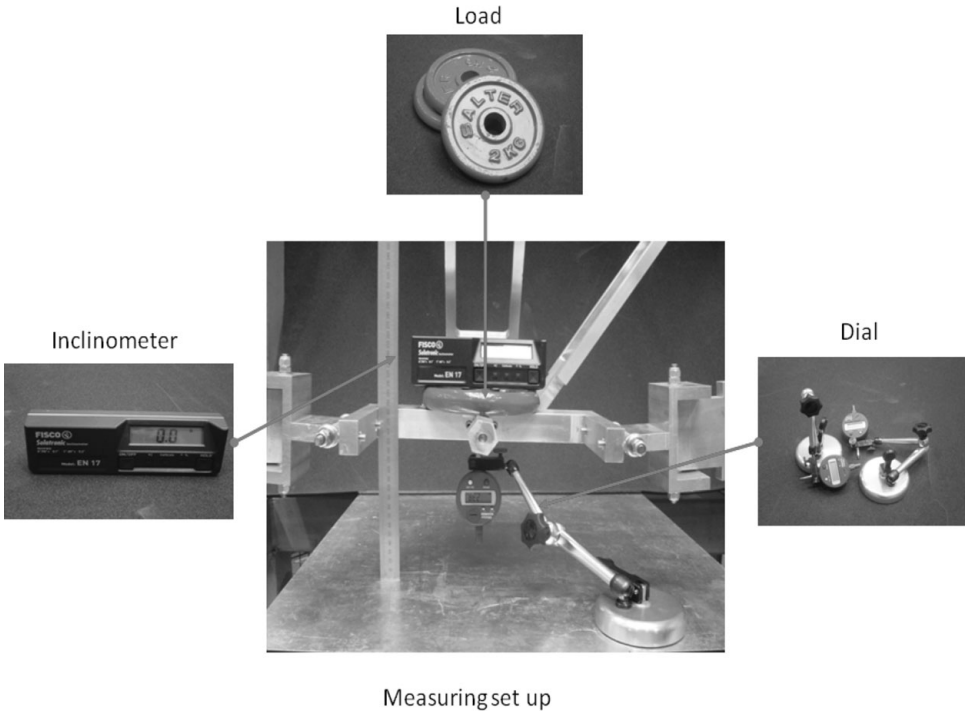


Fig. 16. Experimental set-up and measuring devices.

made in planes of constant height (see Fig. 18). As the manipulator has four DOFs and it is only possible to represent variations of three parameters, first, the stiffness behaviour for constant orientation is evaluated. Subsequently, the measurement position is fixed and the orientation of the mobile platform in the following experimental measurements is varied to consider the evolution of the stiffness based on the orientation of the mobile platform ($k_{zz}(\theta)$). This test of variable orientation is made at the central point ($x = 570$ mm, $y = 663$ mm) of each analysed plane.

From the experimental results, the k_{zz} map for a constant height plane and for a given orientation of the mobile platform is obtained (Fig. 19). The experimental model presents its maximum values for points near the Z- and U-axis, while the minimum values are along the diagonal connecting points 1 and 4 in Fig. 18. The majority of the authors in the literature usually normalize the stiffness results; however, since the main goal of this work is to define a methodology for the stiffness evaluation, the authors of this work have considered it appropriate to not reserve any data and real numerical values of stiffness are presented.

For the other z-constant analysed planes in the workspace, the resulting trends are analogous to the example presented in Fig. 19.

In Fig. 20, the variation of k_{zz} based on the orientation of the actuator is shown. Due to the interference between elements, the turning range of the platform is $\pm 45^{\circ}$. The difference between the maximum value and the minimum is

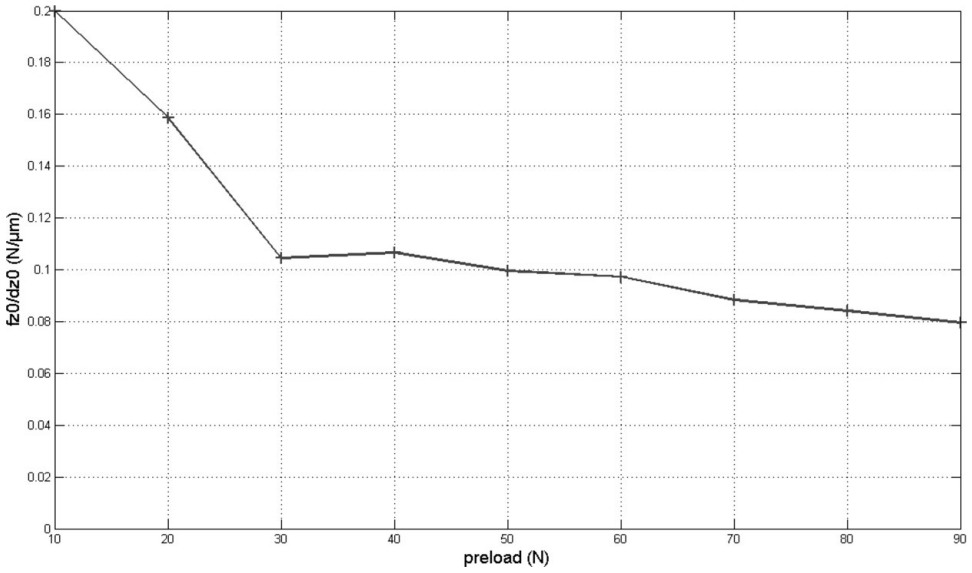


Fig. 17. Preload selection graph.

https://doi.org/10.1017/S0263574709990403 Published online by Cambridge University Press

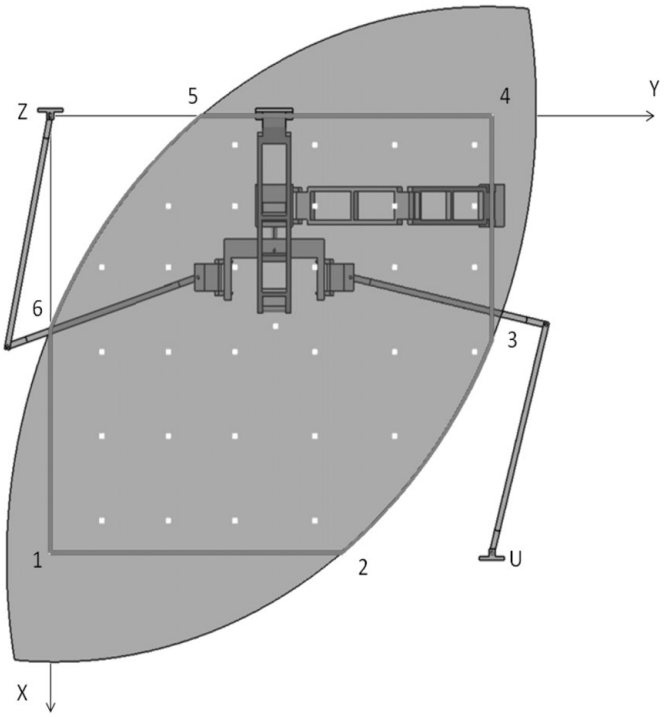


Fig. 18. Measured points in a Z constant plane. Top view.

9%. Given the axial symmetry around the spin axis of the platform the behaviour could be obtained for the values in the range [125°, 235°].

4.3.2. Analytical model. As shown in Fig. 11, the displacements caused in the cross-sectional plane of a vertical load can be considered as negligible, so the model for the complete manipulator can be reduced to those elements that bear the vertical load: the two horizontal legs and the mobile platform. The stiffness of the moving platform is characterized by a simply supported beam with a unitary load applied in its middle point. The resulting displacement is added serially to those affecting the stiffness of each leg. Analytical stiffness behaviour is represented by the two legs mounted in parallel and then serially connected to the mobile platform as depicted in Fig. 21.

In this case, the element k_{zz} that represents the analytical stiffness of the manipulator is obtained as

$$\frac{1}{k_{zz}} = \frac{1}{k_{zz}^{Z} + k_{zz}^{U}} + \frac{1}{k_{zz}^{MP}}, \tag{23}$$

where k_{zz}^{z} and k_{zz}^{U} are the stiffness of the Z and U legs respectively (see Fig. 14) and k_{zz}^{MP} the stiffness of the mobile platform. In Fig. 22, a graph showing the continuous variation of the k_{zz} stiffness element is presented.

The trends that the model shows are analogous to those presented by the prototype, with the maximum values at points near Z- and U-axis, and a valley corresponding to the diagonal which connects points 1 and 4 in Fig. 18. For the points in the XY plane close to the Z- and U-axis, the stiffness increases significantly because low values of the alpha parameter are reached for one of the legs.

4.3.3. Finite element-based model. For the study of the static stiffness behaviour of the manipulator by means of the FEM, a numerical model of the DAEDALUS I manipulator was created from the CAD geometry used in its design. Like in the experimental study, for the constant orientation case, the same analyses carried out in the experimental stage have been repeated for the FEM study. The FEM model (Fig. 23) is defined with 126,000 parabolic tetrahedral elements. The boundary conditions with the fixed element are two clampings. For all the rotational joints, kinematic restraints

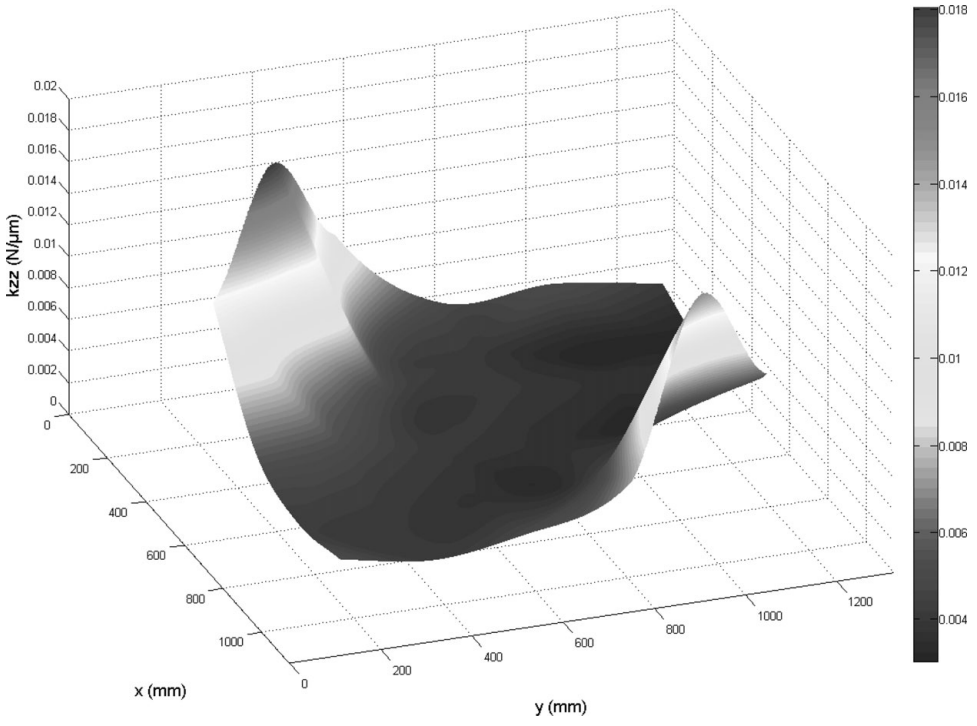


Fig. 19. Experimental k_{zz} (N/µm) for $Z = 150$ mm and $\theta = 0°$.

https://doi.org/10.1017/S0263574709990403 Published online by Cambridge University Press

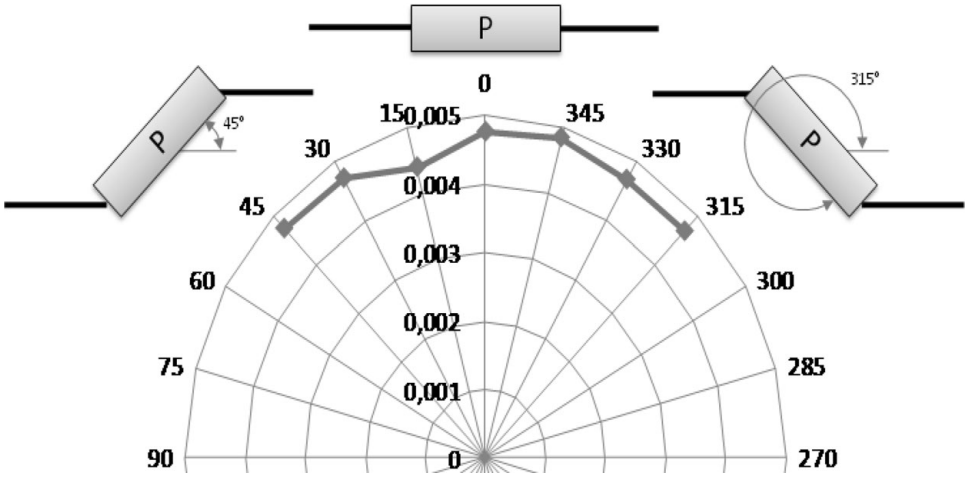


Fig. 20. Experimental $k_{zz}(\theta)$ (N/μm).

have been imposed so that the static behaviour can be analysed.

Figure 24, the k_{zz} component for constant orientation is shown. Again, the maxima appear for points close to the *Z*- and *U*-axis, while minimum stiffness continues to be found in the valley along the diagonal connecting points 1 and 4. The predicted behaviour agrees with that described by the experimental prototype as well as the analytical model.

The variation based on the orientation of the numerical model appears in Fig. 25. Once again, the trends shown by this model agree with those demonstrated by the prototype. The numerical model forecasts a small variation of the stiffness as a function of the orientation with a difference between the maximum and minimum values of less than 4%. For this model, numerical values of stiffness are smaller but with a constant offset with respect to the experimental response.

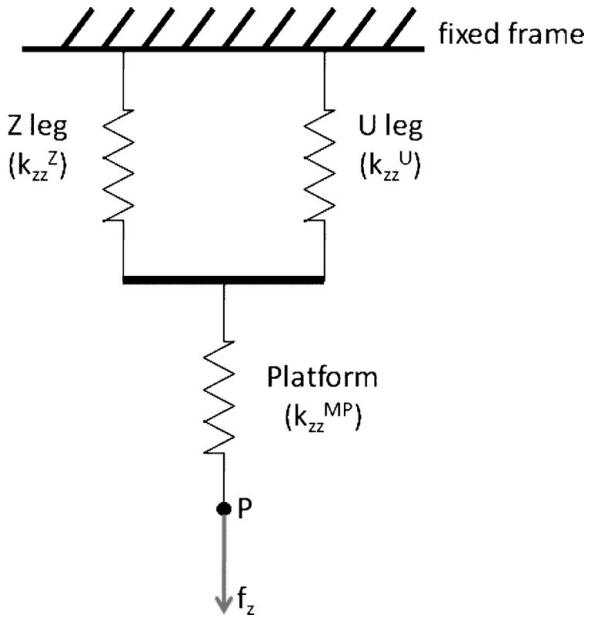


Fig. 21. Stiffness equivalence diagram. Analytic model.

5. Conclusions

From the results of this work, a methodology focused on saving time and effort is proposed. On the one hand, experimental testing is a tedious, time-consuming approach that requires highly accurate and repeatable procedures. This leads to long experimental times and, moreover, measurements may contain errors. On the other hand, the FEM approach needs, in general, a geometrical model that sometimes comes from the design stage. The processing times for the static solution and the redefinition of the mesh for each simulated point turn this task into a costly approach for this kind of multipoint modelling.

As a consequence, some guidelines should be established in order to optimize the stiffness mapping for parallel manipulators. A suggested basis for the procedure is presented in the flowchart in Fig. 26.

The first stage in this chart corresponds to description of the topology of the manipulator. With this data, the number and type of manipulator legs are defined so that the type and number of DOFs are clearly established. In addition, the working mode of the manipulator for the selected task should be identified. In this way, the main characteristics for the simplifying hypothesis are obtained and, in the second stage, the analytical stiffness model is defined in an accurate way. This analytical model gives the stiffness behaviour in the workspace of the manipulator with as many points as necessary. In the third stage, depending on the availability of a prototype and/or an FEM model the various offsets are defined. The key idea is based on obtaining an analytical model with a correct trend, that is, an analytical response as shown at the bottom of Fig. 26 where all the responses have the same trends but are scaled, with an offset. In this case, one experimental measurement or one FEM analysis is sufficient to identify the *ANA/EXP*, *ANA/MEF* or *MEF/EXP* offset. This offset is defined as the constant distance between the reference stiffness response (experiment (I) or FEM-based (II), see Fig. 26) and the analytical one. Once the offset is determined, the real model is obtained by the scaling of the analytical response so that the real stiffness is defined for every point in the workspace.

https://doi.org/10.1017/S0263574709990403 Published online by Cambridge University Press

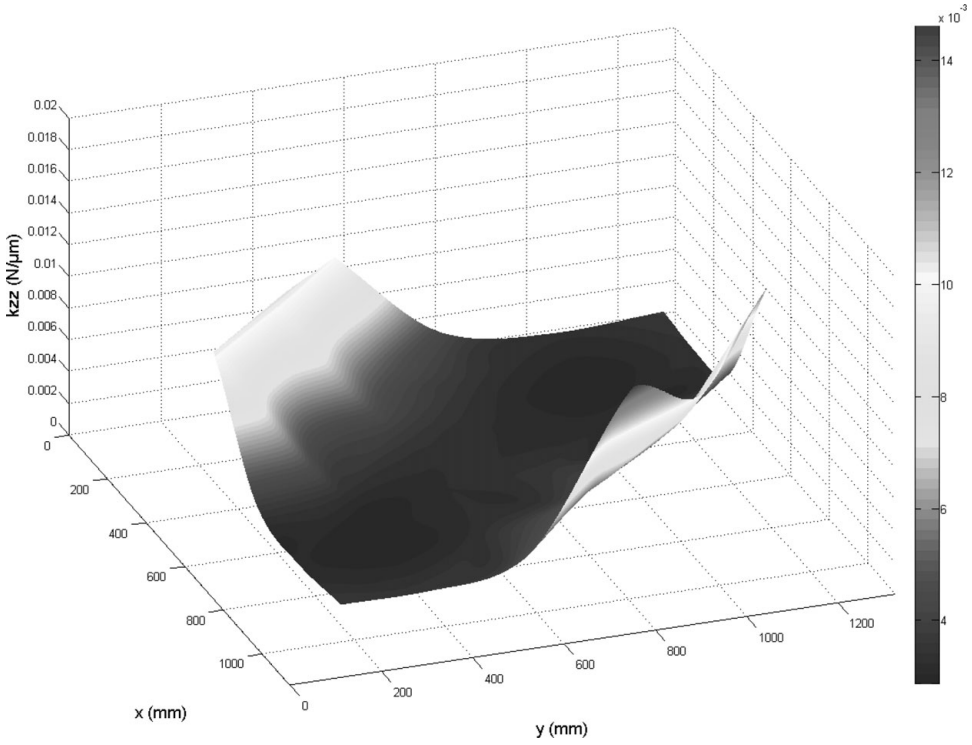


Fig. 22. Analytical k_{zz} (N/μm) for $Z = 150$ mm and $\theta = 0^{\circ}$.

In this work, a methodology for obtaining the stiffness maps by means of two theoretical models and an experimental prototype has been proposed. For its validation, it has been applied to the *R*-dyad which is the kinematic chain of the DAEDALUS I leg. After that, a case study on a 4-DOF (three translations and one rotation) parallel manipulator has been carried out.

In the experimental stage on the *R*-dyad mechanism, the preload concept has been introduced. Its key function is to take into account the gaps in the mechanism. The goal is to obtain the minimum value of the preload which makes the mechanical set-up work in an elastic regime, so that it is possible to predict accurately the displacements originated by the applied load.

In the structural analysis of a single arm of the manipulator, a strong influence of the torsion working mode has been detected, and for this reason future work should include optimization of the design of the arms bearing the torsion torque induced by the applied load.

As a result of the comparison between the models and the experimental prototype of the parallel manipulator the methodology for obtaining the stiffness maps has

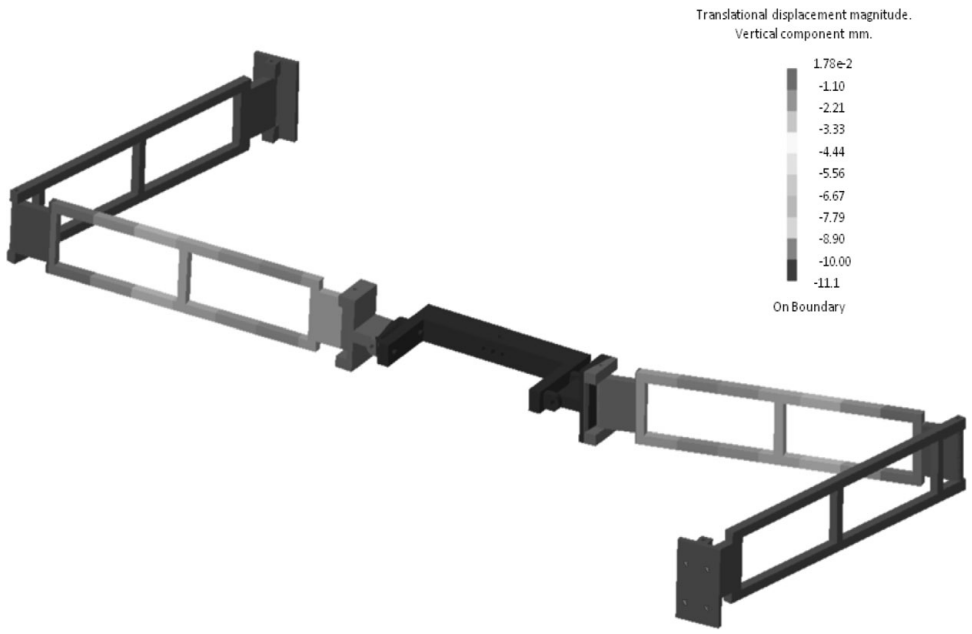


Fig. 23. Vertical displacements field-FEM.

https://doi.org/10.1017/S0263574709990403 Published online by Cambridge University Press

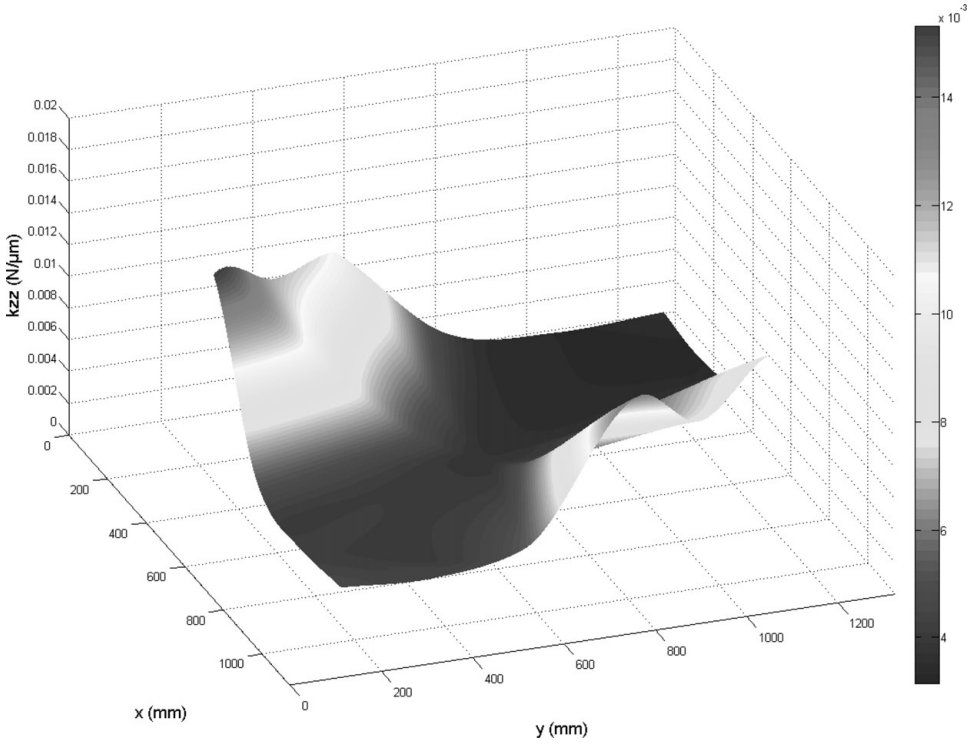


Fig. 24. FEM k_{zz} (N/µm) for $Z = 150$ mm and $\theta = 0°$.

been validated. The difference between the analytical model and the prototype does not exceed 25%, while the agreement between the FEM model and the prototype is greater, with only a 2% error over a wide range of variation. And, as expected, the FEM model is more rigid than the analytical one. In both cases, an analogous behaviour is verified, with the stiffness maxima in the same locations and equivalent variation trends. In this way, it has been demonstrated that it is possible to determine the real static behaviour even by means of the analytical model.

For the whole manipulator behaviour, it should be emphasized that the highest stiffness values are reached for points where one of the legs considered is in its folded configuration and the other completely stretched. Both of these configurations correspond to those predicted by the analytical model to be the most rigid ones. The constant orientation case demonstrates that the model based on the finite elements has an analogous behaviour to the real prototype, being able to predict the variations of k_{zz}. The average error between analytical model and prototype is 8%; and between FEM model and prototype is almost 0%. Considering the high contribution from the assembling errors as well as the backlash, the predicted behaviour is as good in modulus as it is in trends.

In the case of variable orientation with fixed position, the numerical model offers correct trends with respect to the real prototype. In this case, the numerical model has a smaller range of variation than in the experimental case; for the numerical model the rank is only 4% whereas in the prototype the value reaches 9%, but with a constant offset between the two responses.

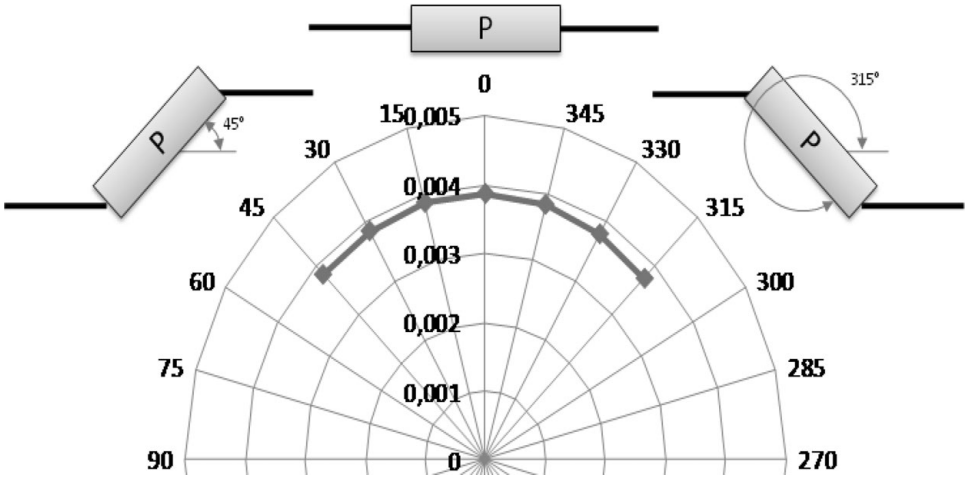


Fig. 25. FEM k_{zz} (θ) (N/µm).

https://doi.org/10.1017/S0263574709990403 Published online by Cambridge University Press

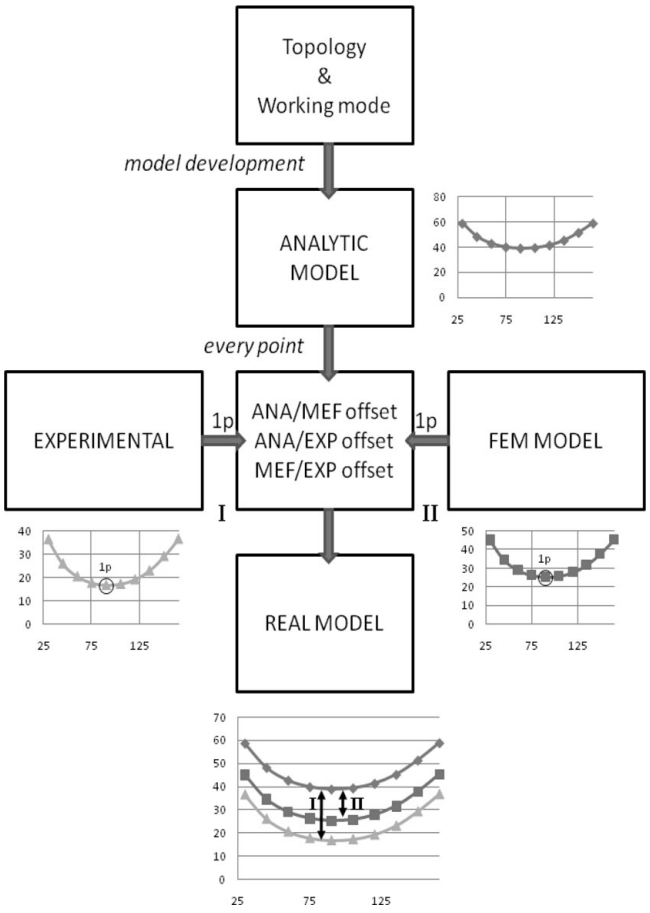


Fig. 26. Procedure stages.

In general terms, from models and prototype results, at least one source of uncertainty is detected: the backlash. In spite of the preload concept, the multiple configurations, as well as the different characteristics of the elements, mean that these gaps are difficult to model.

The proposed methodology has a general applicability for lower mobility parallel manipulators. It introduces an exhaustive analysis on the variations and trends of stiffness as a function of the DOF in the whole workspace. In this paper, a large variation of the stiffness has been demonstrated throughout the workspace, so the analysis in a small area of the workspace could be inadequate. Finally, the stiffness maps here obtained represent a useful tool for the end user of the machine. For a given set of spatial coordinates and mobile platform orientation the stiffness maps allow the correct selection of those zones of the workspace that are most suitable for the stiffness requirements.

Acknowledgements

This work was supported by FEDER funds and the Ministerio de Educación y Ciencia (Spain) DPI2005-02207 and The Basque Country Government GIC07/78 granted projects.

References

1. C. Gosselin, "Stiffness mapping for parallel manipulators," *IEEE Trans. Robot. Autom.* **6**, 377–382 (1990).
2. B. S. El-Khasawneh and P. M. Ferreira, "Computation of stiffness and stiffness bounds for parallel link manipulators," *Int. J. Mach. Tools Manuf.* **39**, 321–342 (1999).
3. C. Gosselin and D. Zhang, "Stiffness analysis of parallel mechanisms using a lumped model," *Int. J. Robot. Autom.* **17**, 17–27 (2002).
4. D. Zhang, F. Xi, C. M. Mechefske and S. Y. Lang, "Analysis of parallel kinematic machine with kinetostatic modelling method," *Robot. Comput.-Integr. Manuf.* **20**, 151–165 (2004).
5. Y. Li and Q. Xu, "Kinematics and Stiffness Analysis for a General 3-PRS Spatial Parallel Mechanism," *Fifteenth CISM-IFToMM Symposium on Robot Design, Dynamics and Control*, Montreal, Canada (2004).
6. O. Company, F. Pierrot and J. Fauroux, "A Method for Modeling Analytical Stiffness of a Lower Mobility Parallel Manipulator," *Proceedings of the 2005 IEEE International Conference on Robotics and Automation*, Barcelona, Spain (2005), pp. 3243–3248.
7. F. Majou, C. Gosselin, P. Wenger and D. Chablat, "Parametric stiffness analysis of the Orthoglide," *Mech. Mach. Theory* **42**, 296–311 (2006).
8. J. Wu, J-J. Wang, L-P. Wang and T-M. Li, "Dexterity and stiffness analysis of a three-degree-of-freedom planar parallel manipulator with actuation redundancy," *J. Mech. Eng. Sci., Proc. IMECH, Part C* **221**, 961–969 (2007).
9. Y. Wang, H. Liu, T. Huang and D.G. Chetwynd, "Stiffness modeling of the Tricept robot using the overall Jacobian matrix," *J. Mech. Robot.* **1**(2), 021002–1-021002–8 (2009).
10. C. Clinton, G. Zhang and A. Wavering, "Stiffness modeling of a Stewart-platform-based milling machine," *Transaction of NAMRI/SME*, Technical Report, Institute for Systems Research (1997).
11. D. Deblaise, X. Hernot and P. Maurine, "A Systematic Analytical Method for PKM Stiffness Matrix Calculation," *Proceedings of the 2006 IEEE International Conference on Robotics and Automation*, Orlando, FL (2006) pp. 4213–4219.
12. Y. Li and Q. Xu, "Stiffness analysis for a 3-PUU parallel kinematic machine," *Mech. Mach. Theory* **43**, 186–200 (2008).
13. T. Huang, X. Zhao and D. J. Withehouse, "Stiffness estimation of a tripod-based parallel kinematic machine," *IEEE Trans. Robot. Autom.* **18**, 50–58 (2002).
14. D. Deblaise and P. Maurine, "Analytical Modeling of Redundant PKM Stiffness Using Matrix Structural Analysis," *Proceedings of the 5th Chemnitz Parallel Kinematics Seminar*, Chemnitz (2006) pp. 155–174.
15. R. Sales and J. C. Mendes, "Stiffness Analysis of a Parallel Manipulator Using Matrix Structural Analysis," *Proceedings of the EUCOMES 08* (2008) pp. 255–262.
16. C. Corradini, J. Fauroux, S. Krut and O. Company, "Evaluation of a 4 Degree of Freedom Parallel Manipulator Stiffness," *Proceedings of the 11th IFToMM World Congress on the Theory of Machines and Mechanisms*, Tianjin, China (2003).
17. Y-W. Li, J-S. Wang and L-P. Wang, "Stiffness Analysis of a Stewart Platform-Based Parallel Kinematic Machine," *Proceedings of the 2002 IEEE International Conference on Robotics and Automation 4*, Washington, DC (2002) pp. 3672–3677.
18. M. Ceccarelli and G. Carbone, "Numerical and experimental analysis of the stiffness performances of parallel manipulators," *Second International Colloquium "Collaborative Research Centre 562"*, Braunschweig, Gerany (2005) pp. 21–35.
19. ANSI/RIA R15.05-1-1990 (R1999), "Evaluation of point-to-point and static performance characteristics of industrial robots and robot systems" (1999).
20. ISO 9283:1998, "Manipulating industrial robots-performance criteria and related test methods" (2003).
21. B5.54, "Methods for performance evaluation of computer numerically controlled machining centers" (2005).
22. P. Ray, "Design of New High Speed Machining Machines," **In** *Product Engineering, Eco-Design, Technologies and Green Energy Part 4* (Springer, The Netherlands, 2006) pp. 379–396.

https://doi.org/10.1017/S0263574709990403 Published online by Cambridge University Press

23. R. O. Kuehl, *Diseño de experimentos: principios estadísticos para el diseño y análisis de investigaciones*, 2nd ed. (Paraninfo, Mexico, 2000).
24. E. Macho, O. Altuzarra, Ch. Pinto and A. Hernández, "Workspaces associated to assembly modes of the 5R planar parallel manipulator," *Robotica* **26**, 395–403 (2008).
25. S. P. Timoshenko and J. N. Goodier, *Theory of elasticity* (URMO, S.A. de Ediciones, New York, 1987).
26. O. Salgado, O. Altuzarra, V. Petuya and A. Hernández, "Type Synthesis of 3T1R Fully-Parallel Manipulators Using a Group-Theoretic Approach," *Proceedings of the 12th IFToMM World Congress*, Besançon, France (2007).
27. ISO 463:2006, "Geometrical Product Specifications (GPS) – Dimensional measuring equipment – Design and metrological characteristics of mechanical dial gauges," ICS: 17.040.30, Stage: 60.60 (2006-02-28), TC/SC: TC 213.

https://doi.org/10.1017/S0263574709990403 Published online by Cambridge University Press